Global Scatterometer Observations of the Structure of Tropical Cyclone Wind Fields

ALI TAMIZI,[a] IAN R. YOUNG,[a] AGUSTINUS RIBAL,[a,b] AND JOSE-HENRIQUE ALVES[c]

[a] *Department of Infrastructure Engineering, The University of Melbourne, Victoria, Australia*
[b] *Department of Mathematics, Faculty of Mathematics and Natural Sciences, Hasanuddin University, Makassar, Indonesia*
[c] *NOAA/NCEP, College Park, Maryland*

(Manuscript received 13 June 2020, in final form 7 September 2020)

ABSTRACT: A very large database containing 24 years of scatterometer passes is analyzed to investigate the surface wind fields within tropical cyclones. The analysis confirms the left–right asymmetry of the wind field with the strongest winds directly to the right of the tropical cyclone center (Northern Hemisphere). At values greater than 2 times the radius to maximum winds, the asymmetry is approximately equal to the storm velocity of forward movement. Observed wind inflow angle (i.e., storm motion not subtracted) is shown to vary both radially and azimuthally within the tropical cyclone. The smallest observed wind inflow angles are found in the left-front quadrant with the largest values in the right-rear quadrant. As the velocity of forward movement increases and the central pressure decreases, observed inflow angles ahead of the storm decrease and those behind the storm increase. In the right-rear quadrant, the observed inflow angle increases with radius from the storm center. In all other quadrants, the observed inflow angle is approximately constant as a function of radial distance.

KEYWORDS: Hurricanes/typhoons; Remote sensing; Satellite observations

1. Introduction

Defining the surface (10 m) wind speed and direction distribution within tropical cyclones is critical for a range of applications including: storm surge and wave modeling, risk assessment, structural loading, and nearshore flooding. Tropical cyclone–generated storm surge is dependent on the details of the wind field, including the size (Irish et al. 2008), maximum wind speed (Xie et al. 2006), and the asymmetry (Houston et al. 1999). Similarly, the magnitude of ocean waves generated by tropical cyclones also depends on the spatial scale of the storm and maximum wind speed, as well as the velocity of forward movement (Young 2017).

Our understanding of the structure of the surface wind field has been formed from both theoretical and model developments, as well as in situ and remote sensing observations. Full coupled numerical models such as the National Oceanographic and Atmospheric Administration/National Weather Service (NOAA/NWS) Hurricane Weather Research Forecast (HWRF model) (Biswas et al. 2016) and HMON model (Mehra et al. 2018) represent the state of the art in tropical cyclone modeling and forecasting. For many applications, however, simpler parametric vortex models with an assumed asymmetry and inflow angle are commonly used to represent the surface wind field (Holland 1980; Willoughby et al. 2006; Holland et al. 2010). In situ measurements from anemometers on offshore buoys provide direct measurements of wind speed and directions but are limited in geographic distribution and potentially biased by sheltering by waves in large seas in tropical cyclone conditions (Alves and Young 2003; Bender et al. 2010; Jensen et al. 2015). The advent of airborne penetration of tropical cyclones has provided wind field measurements using GPS dropwindsondes (Franklin et al. 2003; Powell et al. 2003; Kepert 2006a,b; Schwendike and Kepert 2008). The point measurement limitations of dropwindsondes has been addressed by aircraft-borne Stepped Frequency Microwave Radiometer (SFMR) measurements (Uhlhorn et al. 2007, 2014). Satellite-based instruments, such as the Advanced Microwave Sounding Unit (AMSU) (Bessho et al. 2006), the L-band microwave radiometer carried on the NASA Soil Moisture Active Passive Satellite (SMAP) (Sun et al. 2019), the CYGNSS constellation (Ruf et al. 2016), and scatterometers (Ueno and Bessho 2011; Klotz and Jiang 2016, 2017) have significantly increased the number of storms observed and the geographic distribution of observations.

A full understanding of the structure and parameter dependence of the two-dimensional tropical cyclone surface wind field requires a very large number of observations, which to date have been lacking. This occurs as we are seeking an understanding of the spatial distribution including magnitude, asymmetry and inflow angle as a function of tropical cyclone parameters, such as central pressure p_0 and velocity of forward movement V_{fm}. Hence, this is a multiparameter problem, requiring very large amounts of data to fully explore the dependence on all these parameters. This study develops such a large composite database from 24 years of scatterometer observations covering all tropical cyclone basins. Through such a database, it is possible to investigate, in detail, the spatial structure of the tropical cyclone surface wind field and its dependence on tropical cyclone wind field parameters.

Following this introduction, section 2 provides a summary of recent observations of tropical cyclone surface wind fields and parametric vortex models. This is followed by section 3, which describes the databases used in the study (scatterometer and IBTrACS). Section 4 presents an analysis of potential biases in

---

Corresponding author: ian.young@unimelb.edu.au

DOI: 10.1175/MWR-D-20-0196.1

the resulting composite scatterometer wind fields due to errors in the assumed tropical cyclone wind field parameters. The results of the study are presented in section 5, with conclusions in section 6.

2. Modeling and observations of the tropical cyclone wind field

Holland (1980) represented the tropical cyclone (TC) radial pressure profile as

$$p = p_0 + \Delta p e^{-(R_m/r)^b}, \qquad (1)$$

where p is the surface pressure at radius r from the storm center, R_m is the radius to maximum winds, Δp is the central pressure drop, and b is an exponent that defines the pressure profile. Holland et al. (2010) used this profile to determine the surface (10 m) wind speed:

$$U_{10} = \left[\frac{100 b_s \Delta p (R_m/r)^{b_s}}{\rho e^{(R_m/r)^{b_s}}}\right]^x, \qquad (2)$$

where ρ is the density of air and the subscript s refers to surface values. Following Holland et al. (2010), b_s can be approximated by

$$b_s = -4.4 \times 10^{-5} \Delta p^2 + 0.01 \Delta p + 0.03 \frac{\partial p}{\partial t} - 0.014 \phi + 0.15 V_{\mathrm{fm}}^{x_a} + 1.0, \qquad (3)$$

where Δp has units of hectopascals, $\partial p/\partial t$ has units of hectopascals per hour, ϕ is the absolute value of the latitude in degrees, and V_{fm} is the velocity of forward movement in meters per second. The exponent, $x_a = 0.6(1 - \Delta p/215)$ and the exponent x in (2) is defined as

$$x = \begin{cases} 0.5 & \text{for} \quad r \le R_m \\ 0.5 + (r - R_m)\dfrac{x_n - 0.5}{r_n - R_m} & \text{for} \quad r > R_m \end{cases}. \qquad (4)$$

In (4), $x = x(r)$ and $x_n = x(r_n)$, which can be determined from (2) if data on the surface wind speed is available at a radius r_n from the storm center. Below, we use this model to assess potential errors in our analysis. In these applications, we use $r_n = R_{34}$, the radius to gales where $U_{10} = 17.5\,\mathrm{m\,s^{-1}}$ (34 kt). Hence, the wind speed U_{10} can be determined from (2) if values of R_m, R_{34}, Δp, and V_{fm} are available.

Generally, such parameters can be obtained from best track archives, such as IBTrACS (see below) (Knapp et al. 2018). To complete the model, it is necessary to assume some asymmetry for the wind field and an inflow angle. In the present context, we assume first-order asymmetry by simply adding the velocity of forward movement vector V_{fm} to the vortex wind vector defined by (2) and assuming the maximum is right (Northern Hemisphere) of center (Xie et al. 2006; Hu et al. 2012). Following Shea and Gray (1973) and Zhang and Uhlhorn (2012) a constant observed inflow angle of 20° has been assumed. Both the asymmetry and inflow angle will be explored in detail from the scatterometer database compiled for this study.

Note, in the literature, two definitions of inflow angle are reported. The observed inflow angle is the value that would result from an instantaneous observation of the spatial tropical cyclone wind field, such as from a scatterometer overpass. Alternatively, the storm-relative inflow angle is the value relative to the translating tropical cyclone. That is, the storm-relative value is obtained by the vector subtraction of the velocity of forward movement from the wind field. As the different definitions can lead to confusion, we use the full terms ("observed inflow angle" and "storm-relative inflow angle") throughout the paper and present results for both quantities.

The NOAA Hurricane Research Division (HRD) Real-time Hurricane Wind Analysis System (H*Wind) (Powell et al. 1998; DiNapoli et al. 2012) is a software application used by NOAA's HRD to create a gridded tropical cyclone wind analysis based on a wide range of observations. These observations include aircraft data from SFMR and GPS dropwindsondes, satellite scatterometer observations and in situ ship and buoy data. The final H*Wind analysis product is a gridded wind speed and direction dataset, with historical North Atlantic hurricanes archived at https://www.rms.com/event-response/hwind. As such, H*Wind gridded wind fields provide a composite reanalysis representation of the spatial wind fields within recent North Atlantic Hurricanes.

As data from airborne and satellite systems have increased, a number of studies have examined both the asymmetry and wind inflow angle for composite datasets of multiple tropical cyclones. Zhang and Uhlhorn (2012) considered data from 1600 dropwindsondes taken during 187 flights through 18 hurricanes. They found a mean storm-relative inflow angle of 22.6°. Although there was significant scatter in their results, the composite dataset indicated both radial and azimuthal variations in storm-relative inflow angle as a function of V_{fm}. The largest storm-relative inflow angle (~50°) was found in the right-front quadrant and the smallest storm-relative inflow angle (~10°) was found in the left-rear quadrant. Uhlhorn et al. (2014) considered SFMR data from 128 aircraft missions through 35 hurricanes. The data suggested there was no increase in surface wind speed asymmetry with increasing V_{fm}, contrary to conventional understanding. Ueno and Bessho (2011) considered QuikSCAT scatterometer data from 252 transects over 62 typhoons, while Klotz and Jiang (2016, 2017) considered global scatterometer data from QuikSCAT and OCEANSAT for the period 2000–11. These analyses confirmed the left–right asymmetry was a function of V_{fm} but also found a strong dependence on vertical shear. Sun et al. (2019) used SMAP data from 125 passes over 43 tropical cyclones over the period 2015–17 to examine the dependence of asymmetry on V_{fm} and vertical shear. They found that asymmetry increased with increasing V_{fm} and decreased with increasing Δp.

The above analyses show the value of pooling multiple tropical cyclones to form a composite dataset. As noted above, however, they highlight the need for very large datasets to cover the full 2D spatial domain, as well as the potential dependence on parameters such as V_{fm}, Δp(or p_0), r, and possibly other parameters such as vertical shear. This requirement for such very large datasets provides the impetuses for this study, which pools data from 24 years of global scatterometer observations.

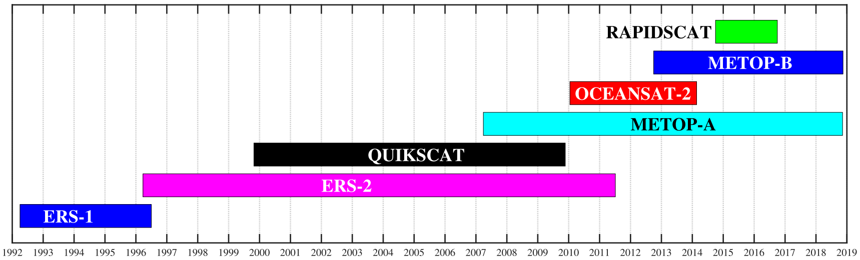

FIG. 1. The durations of the scatterometer missions in the Ribal and Young (2020) database. Tropical cyclone data were extracted from this database. Note that *ERS-1* data were not analyzed, as IBTrACS data for this period do not include all necessary TC wind field parameters.

3. Datasets

Ribal and Young (2020) have compiled a quality controlled composite dataset of the main scatterometer missions that have been operational since 1992. These missions include (in order of launch) *ERS-1*, *ERS-2*, QuikSCAT, *MetOp-A*, *OCEANSAT-2*, *MetOp-B*, and RapidSCAT. The duration of each mission is shown in Fig. 1. This scatterometer dataset was used in conjunction with the International Best Track Archive for Climate Stewardship (IBTrACS) (Knapp et al. 2018) to determine scatterometer passes near tropical cyclones. IBTrACS data were interpolated in time (generally available at 6-h intervals) to the times of scatterometer passes and all scatterometer data within $10R_m$ of the IBTrACS tropical cyclone center location extracted. Note that the Ribal and Young (2020) dataset includes *ERS-1* data. However, for the period of that satellite mission (1992–96), the IBTrACS data does not contain parameters such as R_m and R_{34} hence, data from *ERS-1* were not included in the subsequent analysis.

The full dataset consisted of 13 592 scatterometer passes over 816 tropical cyclones and a total of 14 421 823 observations of surface wind speed U_{10} and direction, (Table 1). The distribution of TCs and scatterometer passes for each of the satellites is detailed in Table 2. Only observations within latitudes of ±35° were considered. Figure 2 shows a contour plot of the relative density of U_{10} measurements. As can be seen, all the major tropical cyclone basins are present, with the largest number of observations from the northwest Pacific.

The Ribal and Young (2020) multiplatform scatterometer dataset has been consistently calibrated and cross validated against buoy and platform data. However, these calibrations are limited to wind speeds less than 30 m s^{-1}. At extreme winds, scatterometers display a low bias due to reduced backscatter signal (Hersbach et al. 2007; Verhoeh et al. 2012). Chou et al. (2013) have compared ASCAT measurements of U_{10} against dropwindsonde data from tropical cyclones. Their data indicate that above 30 m s^{-1}, the scatterometer (ASCAT) data progressively underestimates the dropwindsonde wind speeds and propose a correction relationship:

$$U_{10}^{*} = 0.014U_{10}^{2} + 0.821U_{10} + 0.961. \qquad (5)$$

In (5), U_{10}^{*} is the calibrated wind speed and U_{10}, the 10 m elevation wind speed provided from the standard scatterometer product. Ribal and Young (2020) showed that the calibration relationships across all seven scatterometers in the combined database were quite similar up to the available data limit of 30 m s^{-1}.

We wish to test if (5) is appropriate to apply across all scatterometers in our database under tropical cyclone conditions. As we do not have comprehensive data across all tropical cyclone basins to directly validation results for such a purpose, we initially used the Holland et al. (2010) model [(2)–(4)] as an approximate reference to compare scatterometer measurements. First, however, it is necessary to determine if the Holland model, with the tropical cyclone parameters provided by IBTrACS is a reasonable approximation to the spatial tropical cyclone wind field. To test the Holland model, it was compared to H*Wind wind fields for eight North Atlantic hurricanes: Ivan (2004), Katrina (2005), Rita (2005), Gustav (2008), Ike (2008), Earl (2010), Irene (2011), and Matthew (2016). Figure 3 shows a comparison of the Holland and H*Wind spatial wind fields for Hurricane Ivan. The result shown is typical of the full set of test hurricanes. Typically, the

TABLE 1. Number of tropical cyclones (TCs), scatterometer overpasses, and wind speed observations. Column 1 indicates all data in IBTrACS. Column 2 indicates the data used in the validation of the scatterometer data (as in Fig. 4). Column 3 indicates the data used in the studies of the TC wind fields (Figs. 8–14).

	All TCs in the IBTrACS database	Observations used for validation (Fig. 4): $p_0 < 990$ hPa, $V_{fm} \le 14$ m s^{-1}, valid TC parameters "good" data	Observations used in wind field studies (Figs. 8–14): $p_0 < 980$ hPa, $V_{fm} \le 12$ m s^{-1}, valid TC parameters "good" data
No. of TCs	2602	816	592
No. of overpasses	66 854	13 592	9056
No. of surface wind speed observations	—	14 421 823	9 904 738

TABLE 2. Number of tropical cyclone (TC) observations for each satellite.

Satellite	All surface wind speed observations	Wind speed observations for which there are IBTrACS TC parameters	Observations used for validation (Fig. 4)
ERS-2	3 663 734	2 340 052	2 074 012
QuikSCAT	10 321 133	7 663 709	6 825 860
MetOp-A	1 234 613	1 225 454	1 073 020
OCEANSAT-2	3 204 204	3 120 783	2 830 222
MetOp-B	597 402	567 236	509 604
RapidSCAT	2 344 223	2 288 772	1 109 105
Total	21 540 568	17 206 006	14 421 823

agreement was reasonable with wind speed differences generally less than 15%, and the largest differences due to errors in the IBTrACS locations of the TC center. Note, the aim here is not to try and optimize TC parameters to obtain the best fit. Rather we accept the values provided by IBTrACS and use these in the Holland model [(2)–(4)].

Based on this validation of the Holland–IBTrACS model for this representative set of hurricanes, model wind fields were generated at the respective times of scatterometer passes for all TCs in the database (13 592 passes for 816 TCs). Collocated scatterometer and model values of U_{10} were then extracted and compared for each of the scatterometers. This resulted in a total of 14 421 823 collocations for the full dataset, with the following numbers for each scatterometer [*ERS-2* (2 074 012), QuikSCAT (6 825 860), *MetOp-A* (1 073 020), *OCEANSAT-2* (2 830 222), *MetOp-B* (509 604), and RapidSCAT (1 109 105)] (see Table 2). Only data for which the TC central pressure $p_0 <$ 990 hPa, velocity of forward movement $V_{\mathrm{fm}} < 14\,\mathrm{m\,s^{-1}}$, the IBTrACS database contained all TC parameters, and the scatterometer data were flagged as valid in the Ribal and Young (2020) database were retained. Figure 4 shows example contour density plots for the collocated wind speeds for QuikSCAT and *MetOp-A*. These are typical of all scatterometers. The uncalibrated scatterometer wind speeds underestimate U_{10} compared to the Holland–IBTrACS model above $25\,\mathrm{m\,s^{-1}}$, consistent with the observations of Chou et al. (2013). Application of the Chou et al. (2013) calibration relation (5) significantly improves the agreement between scatterometer and model. At low wind speeds, the scatterometer (calibrated and uncalibrated) overestimate wind speeds compared to the model. These wind speeds are typically from either the eye of the TC or more commonly, near the outer periphery of the storms (i.e., up to $r \approx 10R_m$). At large values of r, it is expected that the model will underestimate the winds, as the vortex is not embedded in any background circulation. In the eye of the storm, one would expect large errors due to potential errors in TC location data from IBTrACS (see section 4). Therefore, the apparent overestimation of the scatterometer (underestimation of the model) in Fig. 4 is as one would expect.

Application of the Chou et al. (2013) calibration for QuikSCAT (in Fig. 4) results in overestimated wind speeds above $25\,\mathrm{m\,s^{-1}}$, while for *MetOp-A* (and all other scatterometers) there was still a slight underestimation. Noting the differences identified in these comparisons and that the Holland model is a relatively simplistic representation of the tropical cyclone wind field, we investigated comparisons between scatterometer data and aircraft SFMR observations. Although such data are only generally available for North Atlantic hurricanes, it represents a valuable validation. SFMR data were obtained from the NOAA HRD archive (https://www.aoml.noaa.gov/hrd/data_sub/hurr.html) for six of the hurricanes considered above: Katrina (2005), Rita (2005), Gustav (2008), Ike (2008), Earl (2010), and Matthew (2016).

Obtaining precise matchups in time between, almost instantaneous, scatterometer passes and aircraft flight plans lasting hours through a translating hurricane is not trivial. All observations were referenced relative to the center of the translating hurricane and rotated such that the storms all have a common direction of forward motion. At the time of each observation (SFMR or scatterometer), the position of the

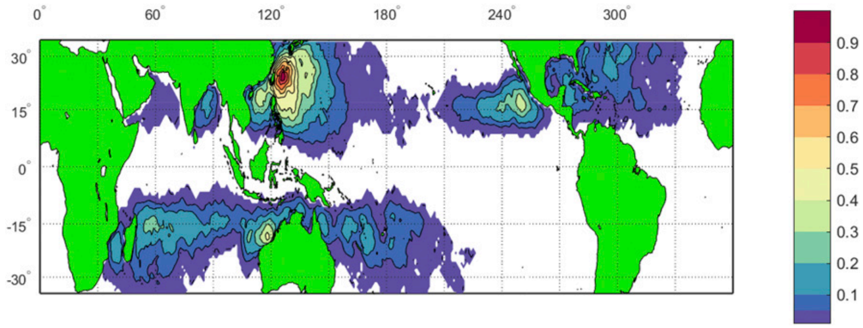

FIG. 2. Relative density of wind speed observations in the global scatterometer tropical cyclone wind field database. The density of observations was normalized such that the maximum density is one.

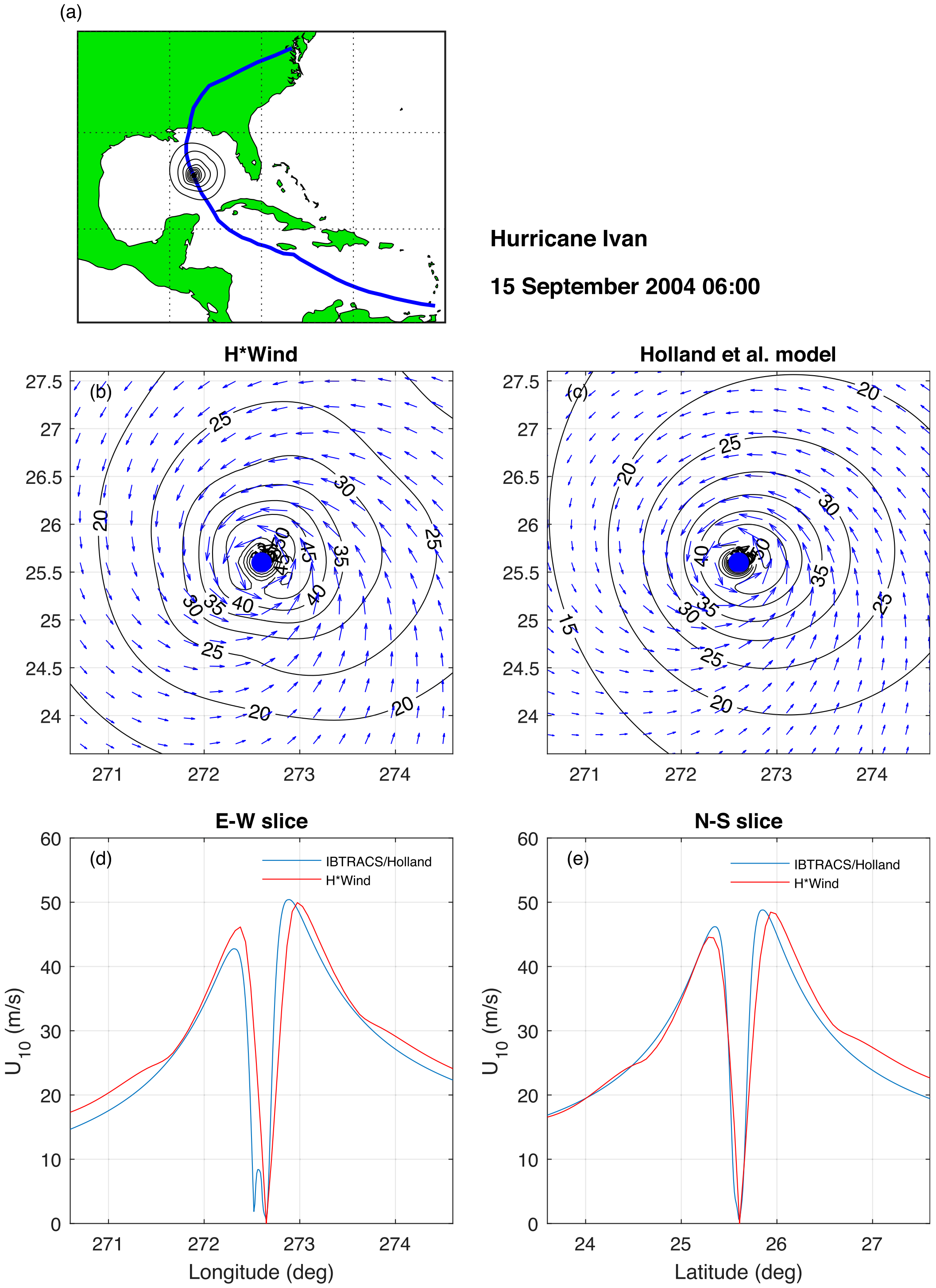

FIG. 3. Comparison between wind fields from the Holland et al. (2010) model with IBTrACS tropical cyclone parameters and H*Wind reanalysis. Results shown for Hurricane Ivan at 0600 UTC 15 Sep 2004. (a) Hurricane track and location, (b) H*Winds wind field, (c) Holland et al. (2010) model wind field, (d) comparison of Holland et al. (2010) model and H*Wind along an east–west slice through the storm center, and (e) as in (d), but along a north–south slice.

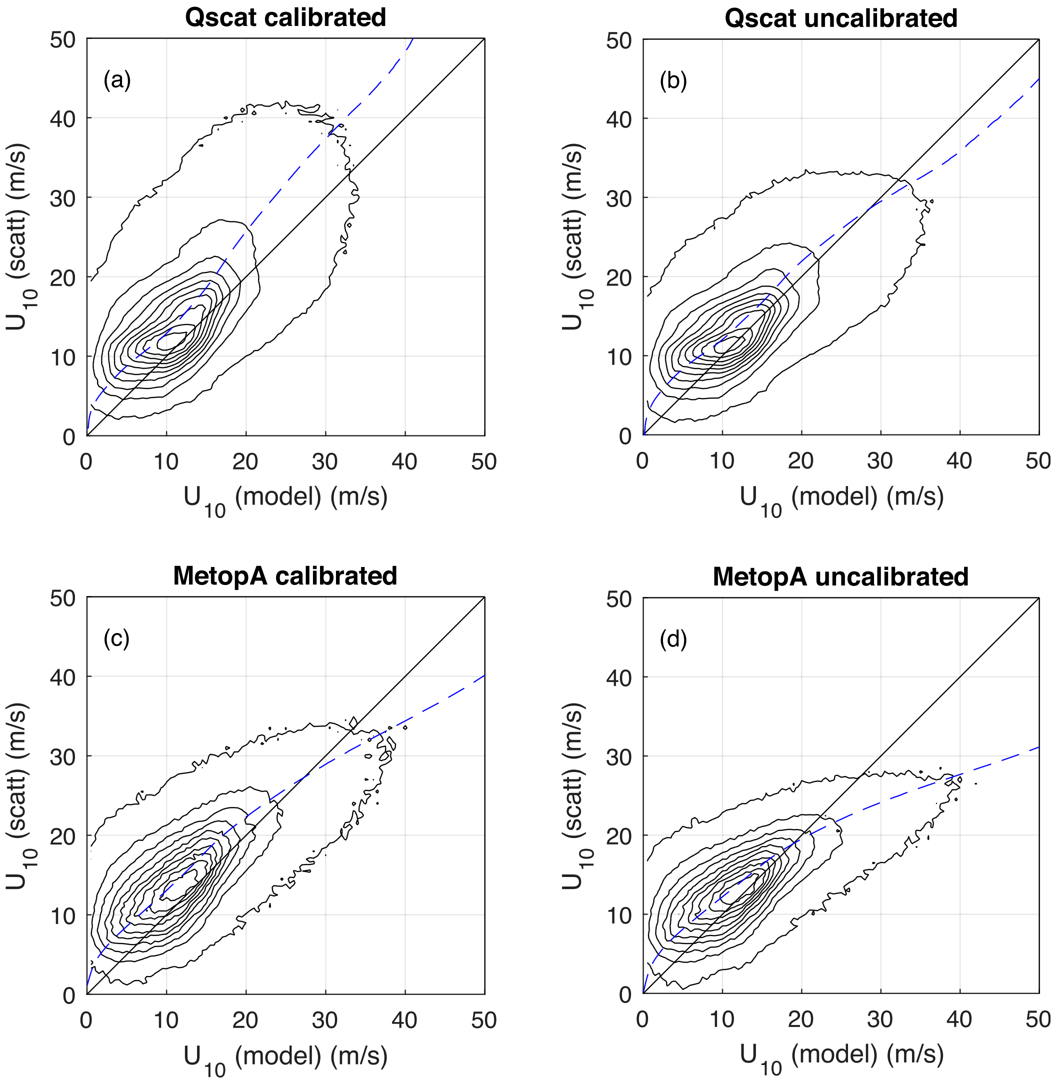

FIG. 4. Comparison between Holland et al. (2010)/IBTrACS model wind speed and scatterometer wind speed. Data are aggregated across the full tropical cyclone database. The contours show normalized density of observations. Contours are drawn at values of [0.9, 0.8, . . .,0.1, 0.01]. (a) Comparison for QuikSCAT data calibrated with Chou et al. (2013) correction (5) and Holland model. (b) As in (a), but with uncalibrated QuikSCAT data. (c),(d) As in (a) and(b), but for *MetOp-A* data.

hurricane was determined by interpolation between positions in the IBTrACS dataset. Note such locations are generally available at 6-hourly intervals. A $0.5R_m \times 0.5R_m$ grid was placed over the hurricane and all observations allocated to the relevant grid square. Only data for which the time mismatch between the SFMR and scatterometer observations were less than 2 h were considered. The median values in each grid square for each 2-h period were then compared. As discussed below in section 4, the finite resolution of the scatterometer footprint potentially biases scatterometer measurements low near the centers of tropical cyclones. (To account for this, the correction described in Fig. 8 was applied to the scatterometer data.)

With the exception of QuikSCAT, the data from all other scatterometers, when corrected using the Chou et al. (2013) relationship (5) produced results in good agreement with SFMR. Consistent with Fig. 4, however, application of the Chou et al. (2013) calibration to QuikSCAT resulted in an overestimation of wind speeds above 25 m s^{-1}. However, the QuikSCAT data without this correction were in good agreement with SFMR data. As a result, the Chou et al. (2013) correction (5) was applied to all scatterometers except QuikSCAT. Figure 5 shows a contour density plot comparing the scatterometer data corrected in this manner [Eq. (5) applied to all scatterometers except QuikSCAT] and SFMR. Similar results were obtained when each scatterometer was considered separately. Figure 5 includes a total of 1957 paired observations of scatterometer and SFMR wind speed. Noting the potential errors caused by

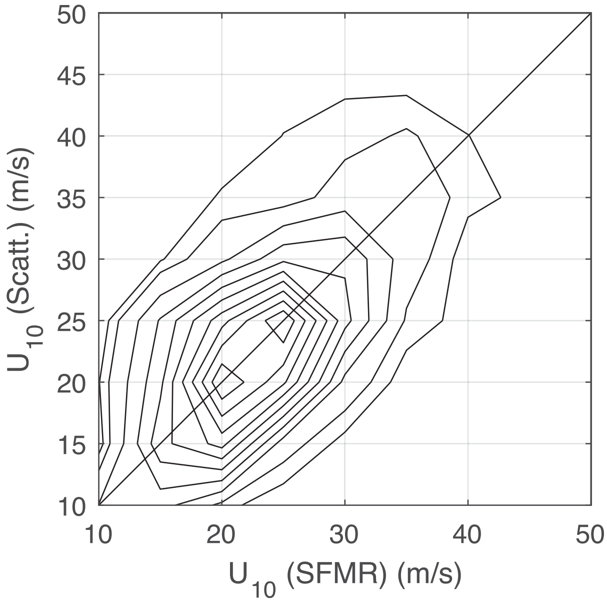

FIG. 5. Comparison between scatterometer and SFMR wind speed. Data are aggregated for all scatterometers used. All scatterometers except QuikSCAT have been corrected with the Chou et al. (2013) high wind speed relationship (5). Smoothing bias-correction factor S in (6) applied to all scatterometer measurements. The contours show normalized density of observations. Contours are drawn at values of [0.9, 0.8, . . .,0.1, 0.01].

inaccuracies in the IBTrACS locations of the hurricane (see section 4) used to obtain the data ''matchups'' there is, not surprisingly, scatter in the data. Nevertheless, the validation does show that the data are in reasonable agreement and that the agreement extends to at least to 40 m s^{-1}. There are limited data points above 40 m s^{-1}, these points also showing agreement between the two measurement systems with no clear bias.

4. Error analysis and bias correction

A number of studies have examined spatial wind and ocean wave fields within combined datasets of tropical cyclones by adopting a frame of reference relative to the position of the TC center and direction of translation (e.g., Young 1998, 2006; Ueno and Bessho 2011; Zhang and Uhlhorn 2012; Young and Vinoth 2013; Uhlhorn et al. 2014; Klotz and Jiang 2016, 2017; Sun et al. 2019; Tamizi and Young 2020). This same process has been adopted here, with the scatterometer observations being transformed, such that they are referenced relative to the center of the TC, with all storms rotated to have a common direction of forward movement. All Southern Hemisphere storms were flipped left–right, such that they can be combined with Northern Hemisphere data. The location of the TC center, and the wind field parameters, V_{fm}, p_0, Δp, R_m, R_{34}, and θ_{fm} (direction of propagation) were all estimated from the IBTrACS data. Only TCs for which IBTrACS enabled such data to be obtained were used. That is, if for example R_m or R_{34} were missing, these storms were not considered.

As these parameters all have associated errors, it is important to determine the potential magnitude of the errors and whether they are distributed symmetrically around the mean value or introduce a systematic bias in the wind estimates. To estimate the magnitude of such errors, we again used the Holland et al. (2010) model. A Monte Carlo simulation was undertaken where each of the main model wind field parameters was allowed to randomly vary around mean values and the resulting 2D wind fields determined. The model was run with the following mean values for the wind field parameters: $p_0 = 950$ hPa, $\Delta p = 60$ hPa, $R_m = 35$ km, $R_{34} = 250$ km, and $V_{\mathrm{fm}} = 5$ m s^{-1}. It was then assumed that: TC location (x_0, y_0), p_0, V_{fm}, and R_m were normally distributed random variables with standard deviations given by: $\sigma_{x_0,y_0} = R_m$, $\sigma_{p_0} = 2.5$ hPa, $\sigma_{V_{\mathrm{fm}}} = 1.0$ m s^{-1}, and $\sigma_{R_m} = 7.5$ km, respectively. A total of 10 000 realizations of the wind field were generated and at each x, y location of the wind field, the mean and the 5th- and

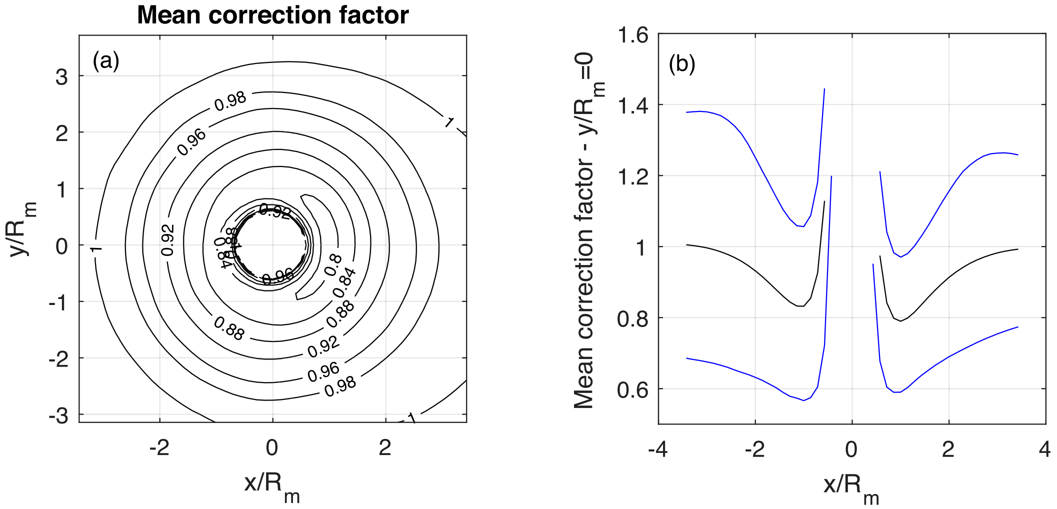

FIG. 6. Bias-correction factor P in (6) for tropical cyclone scatterometer wind speed data due to potential errors in IBTrACS wind field parameters. (a) Mean bias-correction factor as a function of spatial position (x/R_m, y/R_m). (b) Mean and 90% confidence interval for bias correction, along the x/R_m axis in (a) at the value $y/R_m = 0$.

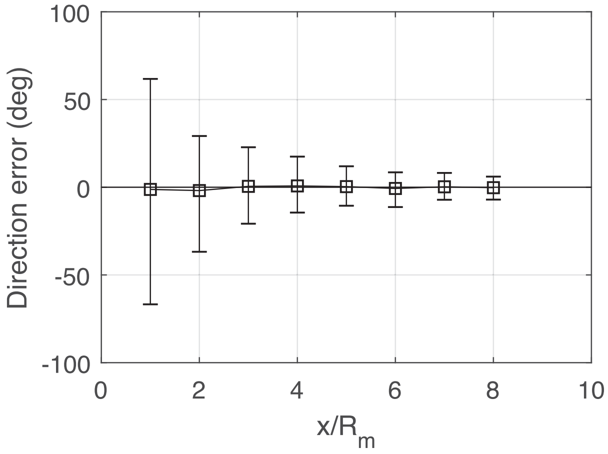

FIG. 7. Mean error for scatterometer observed wind direction data due to potential errors in IBTrACS wind field parameters. Results shown along the x/R_m axis at the value $y/R_m = 0$. The error bars show the 90% confidence interval.

95th-percentile values (90% confidence interval) of the 10 000 realizations of the wind speed U_{10} were determined.

Figure 6a shows the resulting values of the ratio $\overline{U}_{10}/U_{10}(0)$, where $\overline{U}_{10}$ is the mean value from the Monte Carlo simulation and $U_{10}(0)$ is the model wind speed with the mean values of each parameter. As can be seen, these values are always less than one, indicating the winds are biased low because of errors in the wind field parameters. It is errors in the location (x_0, y_0) of the TC center that account for this bias. Variability of the other wind field parameters result in errors symmetrically spread around $U_{10}(0)$. However, the center position error always biases values low. One can understand this by considering the location $x/R_m = 1$ to the right of the storm. This is the position of the wind speed maximum. Any error in the position of the TC center will always result in a lower wind speed at this location. Hence, it has the largest negative bias. However, at all locations, the bias is less than one. Figure 6b shows the mean bias and the 90% confidence limits along the line $y/R_m = 0$, that is a horizontal line through the center of the storm. Consistent with Fig. 6a, the largest bias is located at $|x|/R_m = 1$. At larger values the bias gradually decreases. There are very large potential errors for $|x|/R_m < 1$ but as the wind speed is extremely small within the eye of the storm this has no practical impact. The results in Fig. 6a were used as a lookup table to correct all scatterometer data, depending on the position relative to the TC center.

Figure 7 shows the corresponding mean and 90% confidence limits for observed inflow angle along the line $y/R_m = 0$. In contrast to the error for wind speed magnitude, the direction has no mean bias. The confidence limits are largest at $|x|/R_m = 1$ and decrease for locations farther from the TC center. It should be noted that the confidence limits in Figs. 6b and 7 are for a single wind speed and direction observation. When averaged across the very large number of observations in the present database, these confidence limits will become very small.

A further potential bias occurs because of the finite (and relatively large) scatterometer footprint (12.5 km for QuikSCAT and 25 km for all other scatterometers) (Brennan et al. 2009). This footprint effectively places a 25 km × 25 km (or 12.5 km) spatial average over the wind field. Again, this was simulated with the same Holland model described above. The result of the 25 km spatial averaging is to again bias the measurements low, as shown in Fig. 8. Figure 8a shows the 2D spatial variation and Fig. 8b shows the bias along the axis $y/R_m = 0$. This results in wind speeds biased low by a maximum of approximately 7% at $|x|/R_m = 1$. Note that the results in Fig. 8 are for a tropical

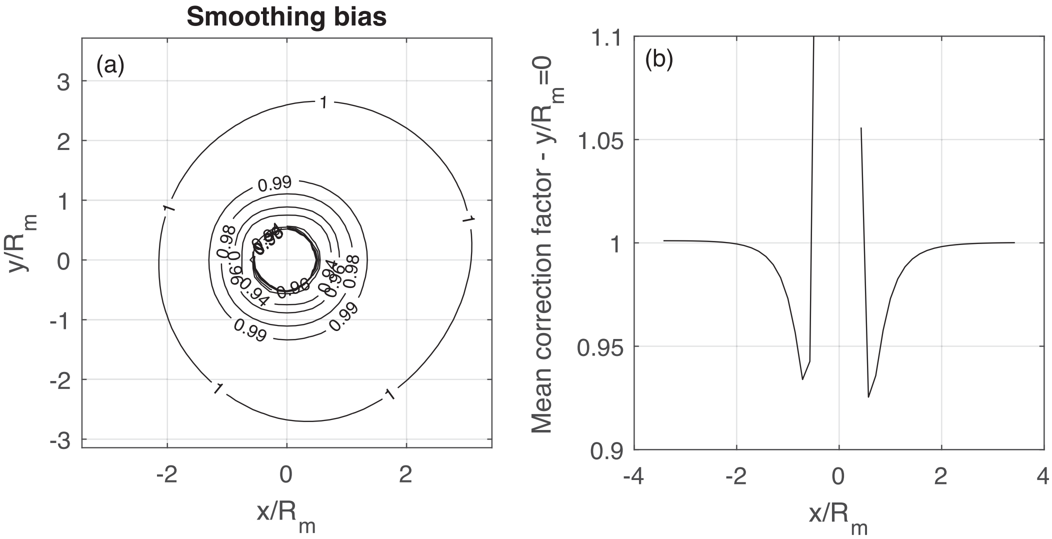

FIG. 8. Smoothing bias-correction factor S in (6) for scatterometer wind speed data due to the 25 km scatterometer footprint. (a) Mean correction factor as a function of spatial position $(x/R_m, y/R_m)$. (b) Mean correction, along the x/R_m axis in (a) at the value $y/R_m = 0$.

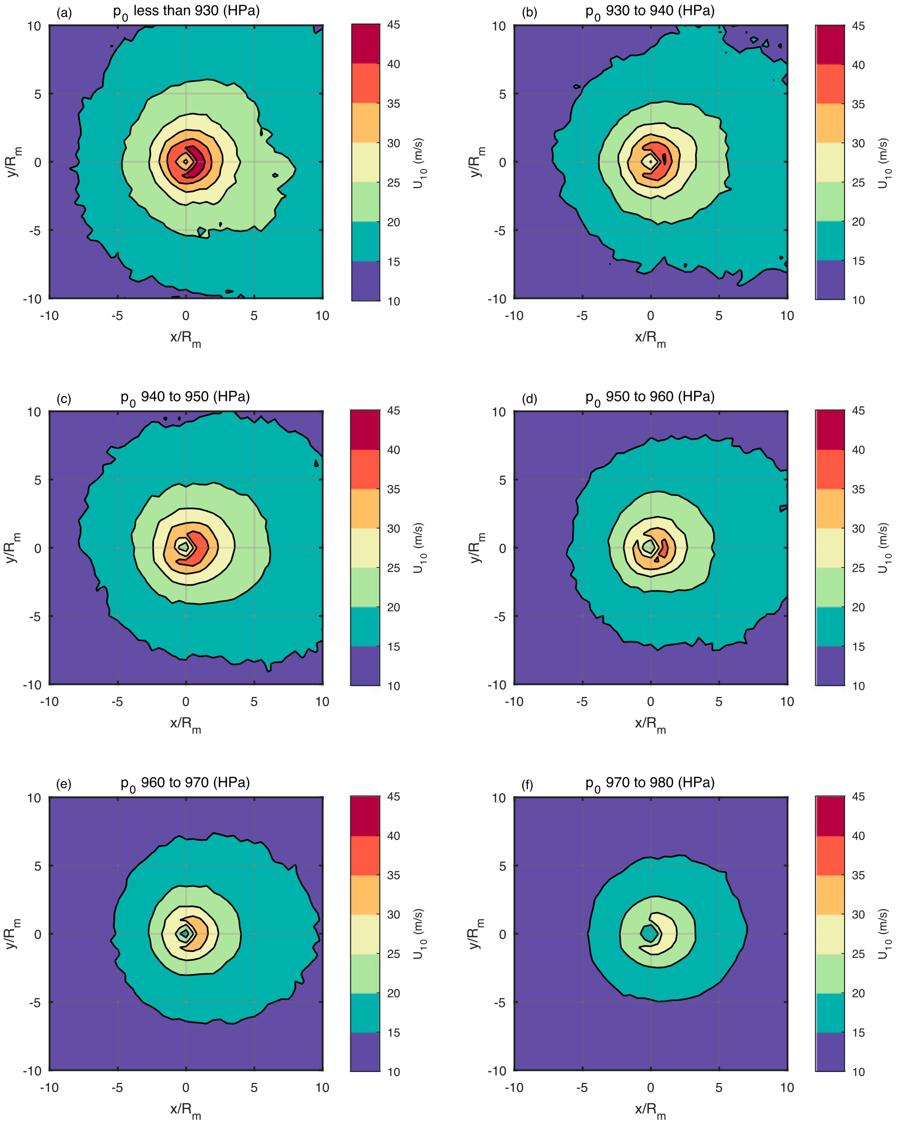

FIG. 9. Contours of tropical cyclone median observed wind speed U_{10} from the full composite dataset of all tropical cyclones. Data are partitioned by central pressure p_0: (a) <930, (b) 930–940, (c) 940–950, (d) 950–960, (e) 960–970, and (f) 970–980 hPa. Data are binned at $0.5R_m \times 0.5R_m$ resolution and tropical cyclone propagating northward (toward the top of the page, or up page).

cyclone with $R_m = 35$ km. This was chosen as a representative value (Kimball and Mulekar 2004), a smaller value of R_m will have larger errors near the TC center and a larger value of R_m will be less impacted. This representative value was used in the scatterometer – SFMR validations and produced acceptable results. In addition, the subsequent analyses (section 5) were repeated excluding all TCs with $R_m < 25$ km, to see if such small storms biased the results. These subsequent results were

TABLE 3. Number of tropical cyclones (TCs), satellite overpasses, and scatterometer wind speed observations for each of the central pressure (p_0) classes considered in Figs. 8 and 14.

	$p_0 < 930$ hPa	$930 \le p_0 <$ 940 hPa	$940 \le p_0 <$ 950 hPa	$950 \le p_0 <$ 960 hPa	$960 \le p_0 <$ 970 hPa	$970 \le p_0 <$ 980 hPa
No. of TCs	116	191	263	331	405	553
No. of overpasses	772	792	1281	1590	1867	2761
No. of U_{10} observation	890 599	885 552	1 410 565	1 793 747	1 965 860	2 958 415

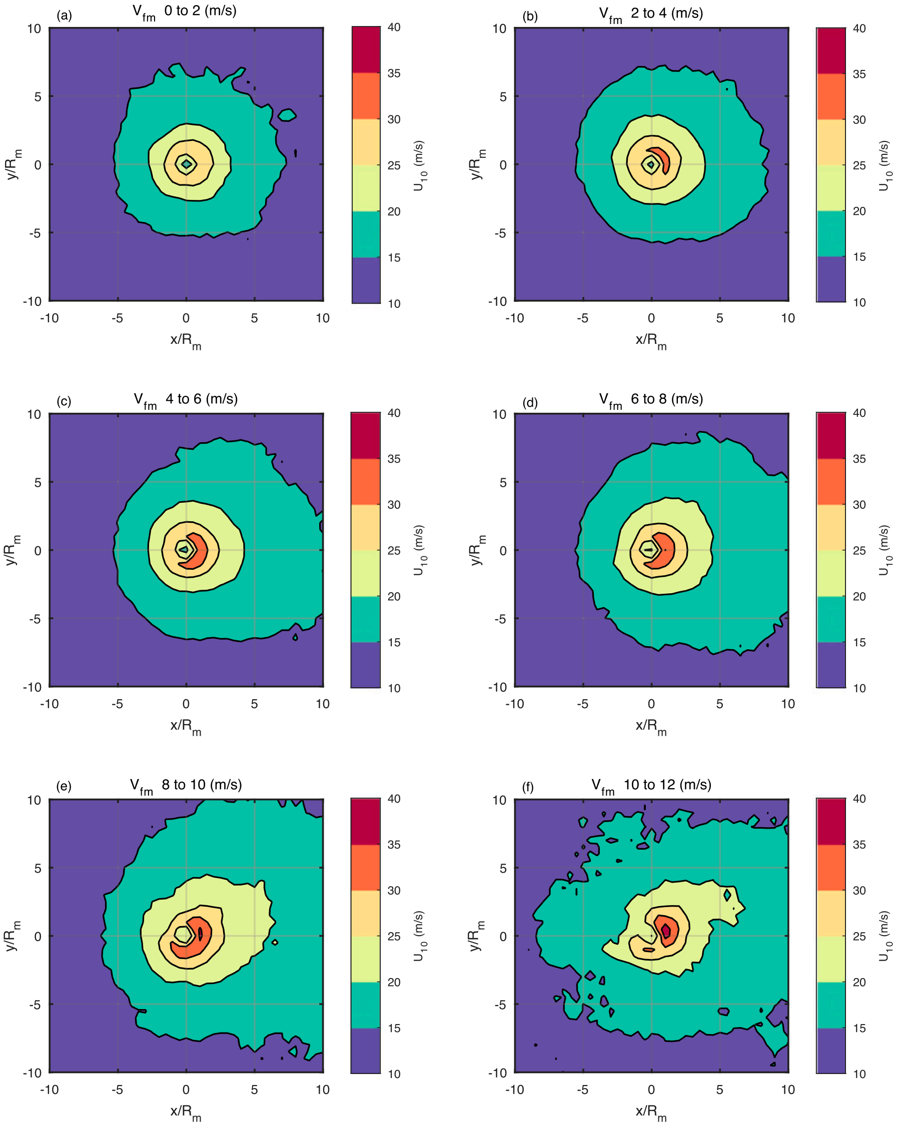

FIG. 10. Contours of tropical cyclone median observed wind speed U_{10} from the full composite dataset of all tropical cyclones. Data are partitioned by velocity of forward movements V_{fm}: (a) 0–2, (b) 2–4, (c) 4–6, (d) 6–8, (e) 8–10, and (f) 10–12 m s^{-1}. Data are binned at $0.5R_m \times 0.5R_m$ resolution and tropical cyclone propagating northward (up page).

negligibly impacted when such small storms were excluded. As a result, we concluded that the above "footprint correction" was a reasonable approximation for the full database, noting the other observational and position errors.

The data in Fig. 8a were again used to provide a bias correction to the scatterometer wind speeds. The final scatterometer wind speeds were bias corrected using the following relationship:

TABLE 4. Number of tropical cyclones (TCs), satellite overpasses, and scatterometer wind speed observations for each of the velocity of forward movement (V_{fm}) classes considered in Figs. 9, 11, and 13.

	$0 < V_{\mathrm{fm}} \le 2$ m s^{-1}	$2 < V_{\mathrm{fm}} \le 4$ m s^{-1}	$4 < V_{\mathrm{fm}} \le 6$ m s^{-1}	$6 < V_{\mathrm{fm}} \le 8$ m s^{-1}	$8 < V_{\mathrm{fm}} \le 10$ m s^{-1}	$10 < V_{\mathrm{fm}} \le 12$ m s^{-1}
No. of TCs	176	396	473	357	212	141
No. of overpasses	682	2482	3063	1762	742	343
No. of U_{10} observation	815 792	2 829 826	3 307 145	1 862 975	746 463	342 537

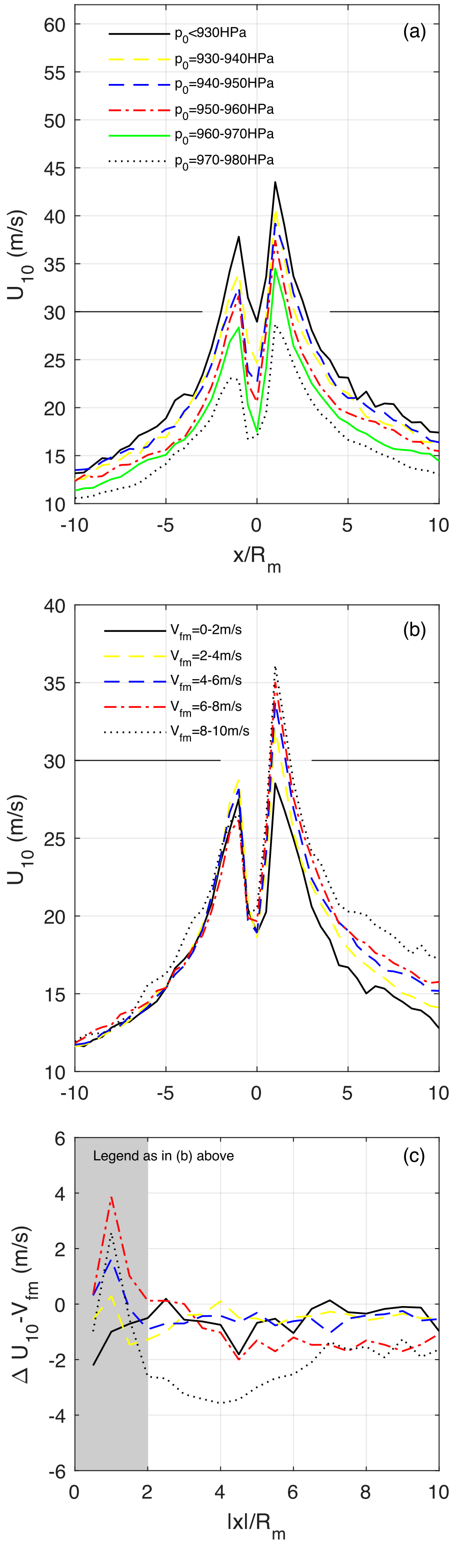

FIG. 11. Tropical cyclone wind field asymmetry from the full composite dataset of all tropical cyclones. (a) Observed wind speed U_{10} along the x/R_m axis at the value $y/R_m = 0$, with data partitioned by central pressure p_0. (b) As in (a), but data partitioned by velocity of forward movement V_{fm}. (c) As in (b), but with $\Delta U_{10}(|x|/R_m) - V_{\mathrm{fm}} = [U_{10}(x/R_m) - U_{10}(-x/R_m)] - V_{\mathrm{fm}}$ as a function of $|x|/R_m$. $\Delta U_{10}(|x|/R_m) - V_{\mathrm{fm}} = 0$ indicates the left–right asymmetry is accounted for by V_{fm}. Shaded area for $|x|/R_m < 2$ shows region in which we have less confidence in the data.

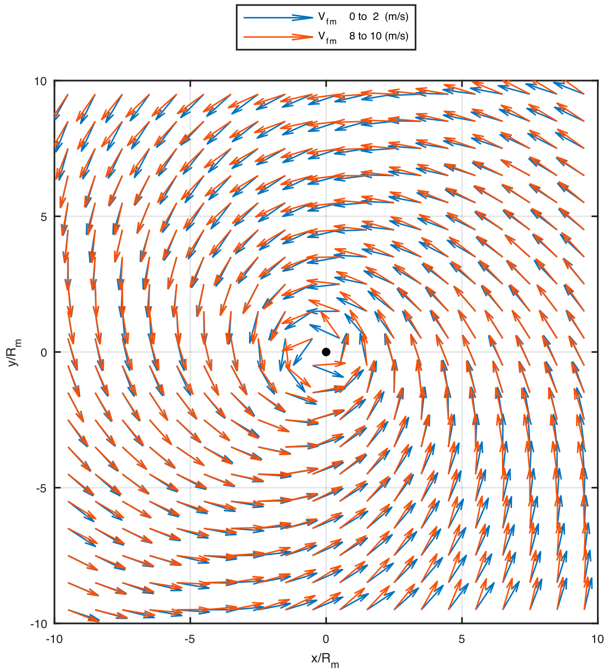

FIG. 12. Tropical cyclone observed wind speed vectors from the scatterometer data for $V_{\mathrm{fm}} = 0$–$2\,\mathrm{m\,s^{-1}}$ (blue) and $V_{\mathrm{fm}} = 8$–$10\,\mathrm{m\,s^{-1}}$ (red). Data are binned at $0.5R_m \times 0.5R_m$ resolution and tropical cyclone propagating northward (up page). Vectors show direction but not magnitude.

$$U'_{10} = U^*_{10}/(PS), \tag{6}$$

where U'_{10} is the bias-corrected scatterometer wind, U^*_{10} is the calibrated scatterometer wind speed from (5), P is the wind field bias error (Fig. 6a), and S is the footprint smoothing bias correction (Fig. 8a). In the case of QuikSCAT, U^*_{10} was not corrected with (5).

Note that for the scatterometer–SFMR validation in section 4, the scatterometer footprint correction, S was applied to the scatterometer data. However, the wind field bias correction, P was not applied as such errors potentially exist in both datasets, due to the need to use the TC-center frame of reference for comparisons.

5. Observed tropical cyclone wind fields

As noted above the data were all placed in a Northern Hemisphere TC centered frame of reference. The data from all scatterometer passes were then pooled and spatially binned into a $0.5R_m \times 0.5R_m$ grid with the TC propagating to the north (top of page in all figures). The results were then further partitioned based on V_{fm} and p_0. In this way, it is possible to investigate the

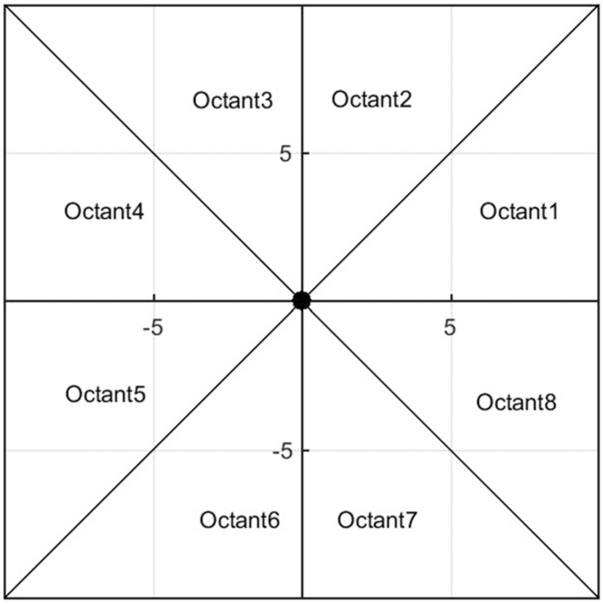

FIG. 13. Diagram showing the naming of the regional octants of the tropical cyclone wind field.

spatial distribution of U_{10}, as well as the asymmetry and wind inflow angle as a function of V_{fm} and p_0.

a. Spatial distribution of wind speed

Figure 9 shows contours of the median gridded values of U_{10} as a function of central pressure p_0. Figure 9 shows $p_0 <$ 930 hPa (Fig. 9a), 930–940 hPa (Fig. 9b), 940–950 hPa (Fig. 9c), 950–960 hPa (Fig. 9d), 960–970 hPa (Fig. 9e), and 970–980 hPa (Fig. 9f). Table 3 provides details of the number of TCs, satellite overpasses and wind speed observations in each of these subclasses. Similarly, Fig. 10 shows the spatial distributions of U_{10} as a function of V_{fm}: $V_{\mathrm{fm}} = 0$–$2\,\mathrm{m\,s^{-1}}$ (Fig. 10a), 2–4 $\mathrm{m\,s^{-1}}$ (Fig. 10b), 4–6 $\mathrm{m\,s^{-1}}$ (Fig. 10c), 6–8 $\mathrm{m\,s^{-1}}$ (Fig. 10d), 8–10 $\mathrm{m\,s^{-1}}$ (Fig. 10e), and 10–12 $\mathrm{m\,s^{-1}}$ (Fig. 10f). Table 4 provides details of the number of TCs, satellite overpasses and wind speed observations in each of these subclasses.

The results confirm our conventional understanding of the TC wind field, with a clear left–right asymmetry of the wind field. The maximum wind crescent is generally directly right of the storm center, although this does move farther into the right-forward quadrant for the fastest moving TCs (Figs. 9e,f). This behavior is consistent with the numerical model results of Shapiro (1983) and Kepert and Wang (2001). Note, all references refer to the Northern Hemisphere. Also, consistent with scatterometer calibrations, the values of U_{10} shown, represent 10-min mean values. These can be approximately converted to 1-min means by the application of a gust factor. A range of values have been proposed, with Powell and Houston (1996), Powell et al. (2010), and Young (2017) recommending a value of approximately 1.11. Other than the binning of data into the $0.5R_m \times 0.5R_m$ grid, no further smoothing of the data has been applied. All values of U_{10} are observed values, that is the velocity of forward movement, V_{fm} is not subtracted.

The relatively smooth distributions of the contours suggest that the large size of the dataset allows such data segregation while producing stable results. The one exception is for the fastest moving storms ($V_{\mathrm{fm}} = 10$–$12\,\mathrm{m\,s^{-1}}$, Fig. 10f), where there are only 343 scatterometer passes over 141 TCs and a total of 342 537 wind observations (see Table 4). This represents a dataset less than half the size of the next smallest subclass. Because of the smaller dataset, the spatial distributions are noisier than other results (Fig. 10f).

b. Wind field asymmetry

Figures 11a and 11b show the left-side versus right-side asymmetries with respect to the forward motion of the storm along $y/R_m = 0$ (i.e., horizontal line through the TC center and the wind field maximum), as a function of p_0 and V_{fm}, respectively. There was no clear dependence of the asymmetry on p_0. However, consistent with Klotz and Jiang (2016, 2017) and Olfateh et al. (2017) there was a dependence on V_{fm}. Figure 11c shows the left–right wind speed difference [i.e. $\Delta U_{10}(|x|/R_m) = U_{10}(x/R_m) - U_{10}(-x/R_m)$] as a function of $|x|/R_m$. The results show that for $|x|/R_m > 2$, the asymmetry is slightly less than the velocity of forward movement V_{fm} (i.e., small negative values). That is, the asymmetry can be approximately accounted for by the translation speed of the storm, as is often applied in vortex models (e.g., Holland 2008). For $|x|/R_m < 2$, however, the asymmetry is greater than V_{fm} (positive values in Fig. 11c). However, some caution should be exercised in interpreting these values for small $|x|/R_m$. As noted earlier, a number of corrections need to be made to the wind fields for small $|x|/R_m$ [Eq. (6)]. These include the Chou et al. (2013) high speed wind speed correction [Eq. (5); all scatterometers except QuikSCAT], the wind field bias correction P, and the smoothing bias correction S. Despite the encouraging, agreements between scatterometer and SFMR observations, confidence in wind speeds above approximately $30\,\mathrm{m\,s^{-1}}$ and for $|x|/R_m < 2$ is less than for other parts of the TC wind field. Therefore, as a guide to the reader, a line at $U_{10} = 30\,\mathrm{m\,s^{-1}}$

TABLE 5. Mean observed inflow angle for each octant (°) as a function of velocity of forward movement (V_{fm}). The octants (1–8) refer to regions shown in Fig. 13.

V_{fm} ($\mathrm{m\,s^{-1}}$)	Octant 1	Octant 2	Octant 3	Octant 4	Octant 5	Octant 6	Octant 7	Octant 8
$0 < V_{\mathrm{fm}} \leq 2$	24.8	21.0	18.5	17.5	20.5	23.53	27.6	27.9
$2 < V_{\mathrm{fm}} \leq 4$	21.7	16.3	15.3	17.6	20.5	24.4	31.2	29.7
$4 < V_{\mathrm{fm}} \leq 6$	20.5	14.2	11.8	16.3	21.3	26.0	35.0	30.33
$6 < V_{\mathrm{fm}} \leq 8$	19.3	13.0	9.6	15.7	22.7	28.6	35.6	29.9
$8 < V_{\mathrm{fm}} \leq 10$	21.0	11.3	5.2	14.5	21.6	27.3	34.6	31.4
$10 < V_{\mathrm{fm}} \leq 12$	22.4	19.2	16.0	20.0	18.3	25.1	35.1	31.0

TABLE 6. Mean observed inflow angle for each octant (°) as a function of central pressure (p_0). The octants (1–8) refer to regions shown in Fig. 13.

p_0 (hPa)	Octant 1	Octant 2	Octant 3	Octant 4	Octant 5	Octant 6	Octant 7	Octant 8
$p_0 < 930$	19.7	14.8	15.2	23.0	25.8	29.2	35.8	32.8
$930 \le p_0 < 940$	19.7	13.7	12.5	20.0	24.7	28.7	37.1	31.2
$940 \le p_0 < 950$	21.7	14.9	14.1	18.7	22.1	27.1	36.3	33.4
$950 \le p_0 < 960$	21.7	14.9	14.3	18.5	22.0	27.0	35.7	32.4
$960 \le p_0 < 970$	21.5	16.7	16.0	20.6	22.1	25.7	34.8	32.1
$970 \le p_0 < 980$	22.0	17.3	16.8	19.3	21.6	25.6	31.6	29.9

has been added to Figs. 11a and 11b and the region for $|x|/R_m < 2$ has been shaded in Fig. 11c. These indicate that we have less confidence in values of $U_{10} > 30\,\mathrm{m\,s^{-1}}$ and for which $|x|/R_m < 2$.

Note that the present analysis does not investigate the dependence of the asymmetry on vertical wind shear within the tropical cyclone. Such an analysis would require data on shear for the full dataset, which is not immediately available. However, the dataset has the capability of such an analysis, which is left for future analysis.

c. *Wind inflow angle*

As for the asymmetry, the wind direction vectors were also binned on a $0.5R_m \times 0.5R_m$ grid. Figure 12 shows the median observed wind direction vectors for two different ranges of V_{fm} ($V_{\mathrm{fm}} = 0$ to $2\,\mathrm{m\,s^{-1}}$ and $V_{\mathrm{fm}} = 8$ to $10\,\mathrm{m\,s^{-1}}$). Again, no additional smoothing has been undertaken in producing this figure. The consistency of the vector fields is remarkable and clearly attests to the very large amounts of data, even when partitioned by V_{fm}. It is clear from Fig. 12 that there are systematic changes in the observed inflow angle as a function of V_{fm}. The distribution partitioned by p_0 produces similar distributions and is not shown here. To describe the distribution of inflow angle in a consistent manner, the spatial wind field has been divided into octants, as shown in Fig. 13. The octants are numbered for 1 to 8, increasing anticlockwise from the horizontal $+x$ axis. Tables 5 and 6 show the mean observed inflow angle in each octant as a function of V_{fm} and p_0, respectively. Similarly, Figs. 14 and 15 show contour plots of the observed inflow angle as functions of V_{fm} and p_0, respectively.

Figure 14 (Table 5) shows that for slowly moving storms ($V_{\mathrm{fm}} = 0$–$2\,\mathrm{m\,s^{-1}}$, Fig. 14a), the observed inflow angle is relatively constant as a function of both azimuth and radial position with a mean value of approximately 22.6°. As V_{fm} increases the observed inflow angles decrease ahead of the storm (octants 2 and 3) and increase behind the storm (octants 6 and 7). At values of $V_{\mathrm{fm}} = 8$–$10\,\mathrm{m\,s^{-1}}$ (Fig. 14e) the observed inflow angle is clearly a minimum of approximately 5°–10° for octants 3 and 4 (left-forward quadrant) and a maximum of approximately 30°–35° in octants 7 and 8 (right-rear quadrant). The changes in observed inflow angle as a function of V_{fm} change in a consistent manner in Fig. 14, clearly showing the functional dependence.

For octants 1 to 6, the contours radiate out from the center of the TC, indicating that the observed inflow angle is approximately constant as a function of radial distance from the center. In octants 7 and 8 (right-rear quadrant), the observed inflow angle increases as a function of radial distance, r.

As noted earlier, the fastest moving storm partition ($V_{\mathrm{fm}} = 10$–$12\,\mathrm{m\,s^{-1}}$) contains significantly less data and, as a result, is noisier and does not conform as well to the transition described above.

The corresponding values of storm-relative inflow angle (i.e., with V_{fm} subtracted from the observed velocity vectors) are shown in Figs. 16 and 17, partitioned by V_{fm} and p_0, respectively. In Figs. 14 and 15 the range of magnitudes of observed inflow angles (maximum − minimum) are relatively constant across the partitions, although the spatial distribution changes. In contrast, Fig. 16 shows that as V_{fm} increases the range of storm-relative inflow angles increases. That is, the minimum values decrease and the maximum values increase. For the slowest moving storms ($V_{\mathrm{fm}} = 0$ to $2\,\mathrm{m\,s^{-1}}$) (Fig. 16a) the values of storm-relative inflow angle are, not surprisingly, similar to the observed inflow angles (Fig. 14a). As the velocity of forward movement increases, however, the maximum storm-relative inflow angles increase in magnitude to values as large as 65° and move to the right-front quadrant (Fig. 16f). The minimum storm-relative inflow angles decrease to a minimum of −10° (i.e., an outflow) and move to the left-rear quadrant. Note that Fig. 16 uses the same color contour levels as Figs. 14, 15, and 17. However, the lowest and highest levels range from 5° to the minimum value and 40° to the maximum value, respectively. This approach was used to aid comparison with the other figures.

The magnitudes of the values shown in Fig. 14 are broadly consistent with the much smaller previous datasets. Powell (1982) found a mean inflow angle of 22°, with the largest values in the right-rear quadrant and the smallest values in the left-front quadrant, as seen in the present data. Zhang and Uhlhorn (2012) again reported a mean value of 22.6° for the storm-relative inflow angle with values varying between 10° and 50°. Consistent with the present results, Zhang and Uhlhorn (2012) show the maximum values of the storm-relative inflow angle in the right-rear quadrant for slow moving storms, rotating to the right-front quadrant with increasing V_{fm} (see Fig. 16 for comparison). Shapiro (1983) and Nolan et al. (2020, manuscript submitted to *Mon. Wea. Rev.*) propose theoretical reasons why the maximum storm-relative inflow angles should be in the right front quadrant and support this with model simulations.

Figure 15 (Table 6) shows that for the least intense storms ($p_0 = 970$–980 hPa, Fig. 15f), the observed inflow angle is relatively constant as a function of azimuth. As the intensity increases (p_0 decreases) the observed inflow angles in octants 2 and 3 (ahead of the storm) gradually decrease and the values in octants 7 and 8 (right-rear quadrant) gradually increase.

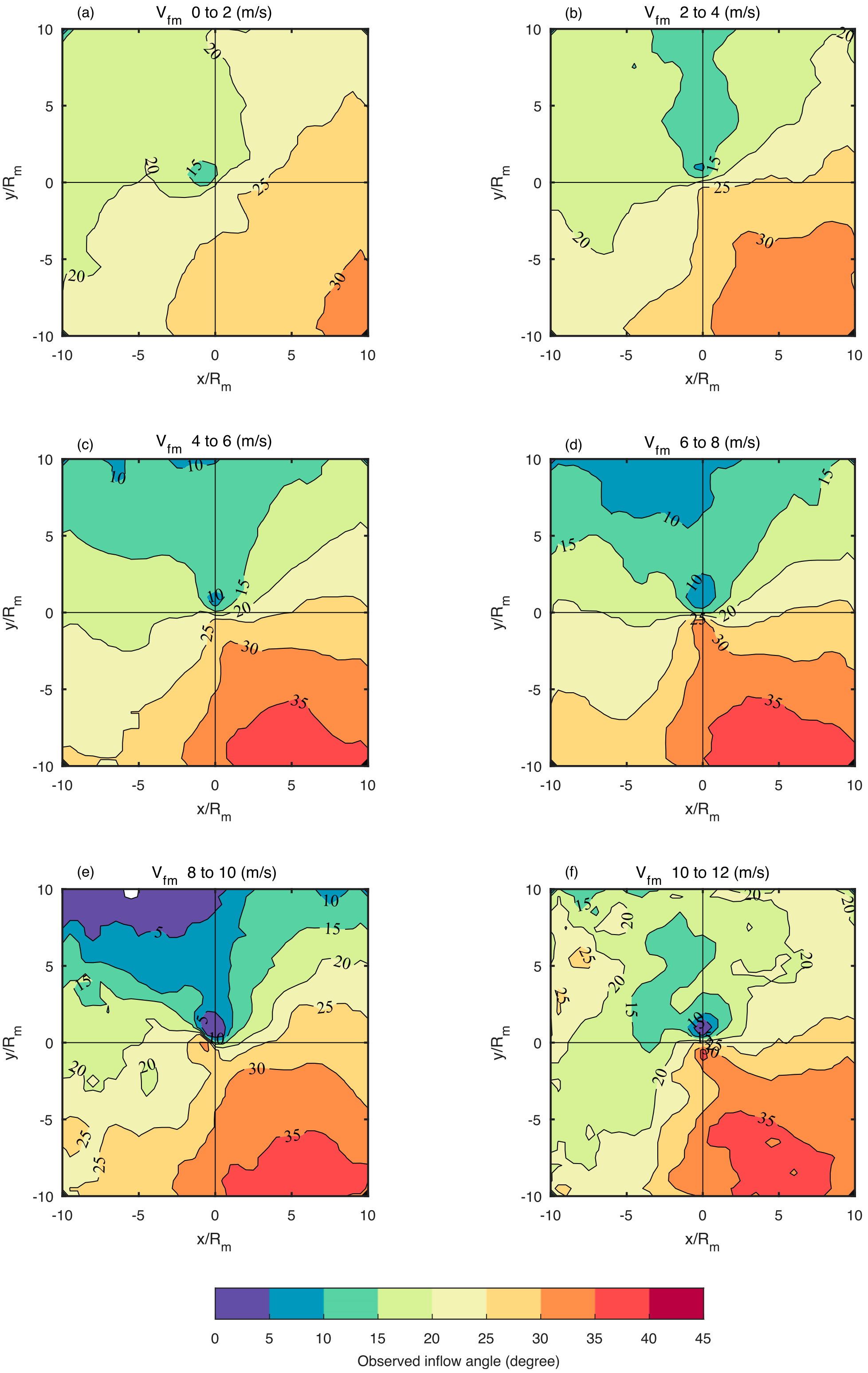

FIG. 14. Contours of tropical cyclone observed wind inflow angle (°) from the full composite dataset of all tropical cyclones. Data are partitioned by velocity of forward movement V_{fm}: (a) 0–2, (b) 2–4, (c) 4–6, (d) 6–8, (e) 8–10, and (f) 10–12 m s^{-1}. Data are binned at $0.5R_m \times 0.5R_m$ resolution and tropical cyclone propagation northward (up page).

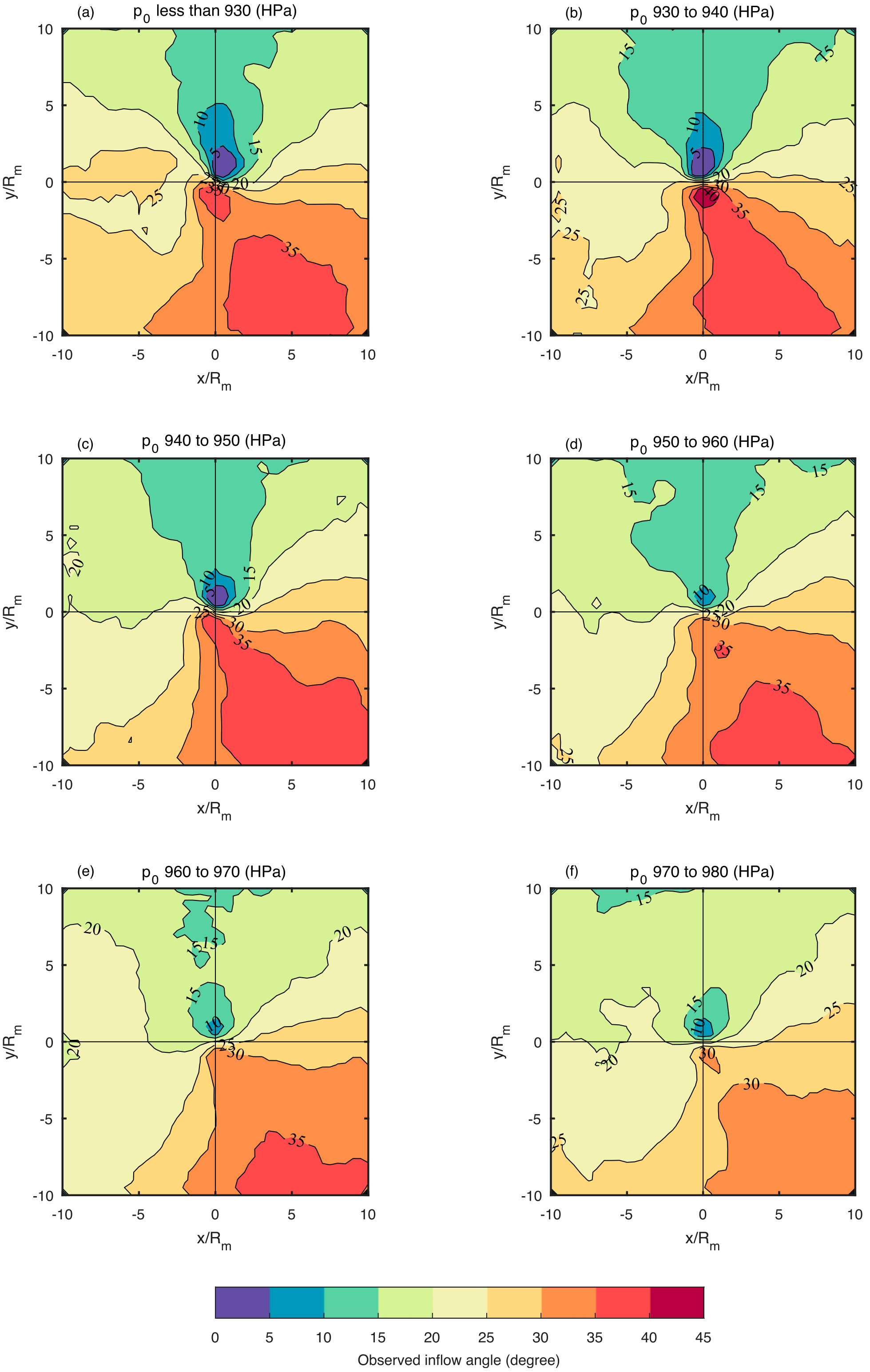

FIG. 15. Contours of tropical cyclone observed wind inflow angle (°) from the full composite dataset of all tropical cyclones. Data are partitioned by central pressure p_0: (a) <930, (b) 930–940, (c) 940–950, (d) 950–960, (e) 960–970, and (f) 970–980 hPa. Data are binned at $0.5R_m \times 0.5R_m$ resolution and tropical cyclone propagation northward (up page).

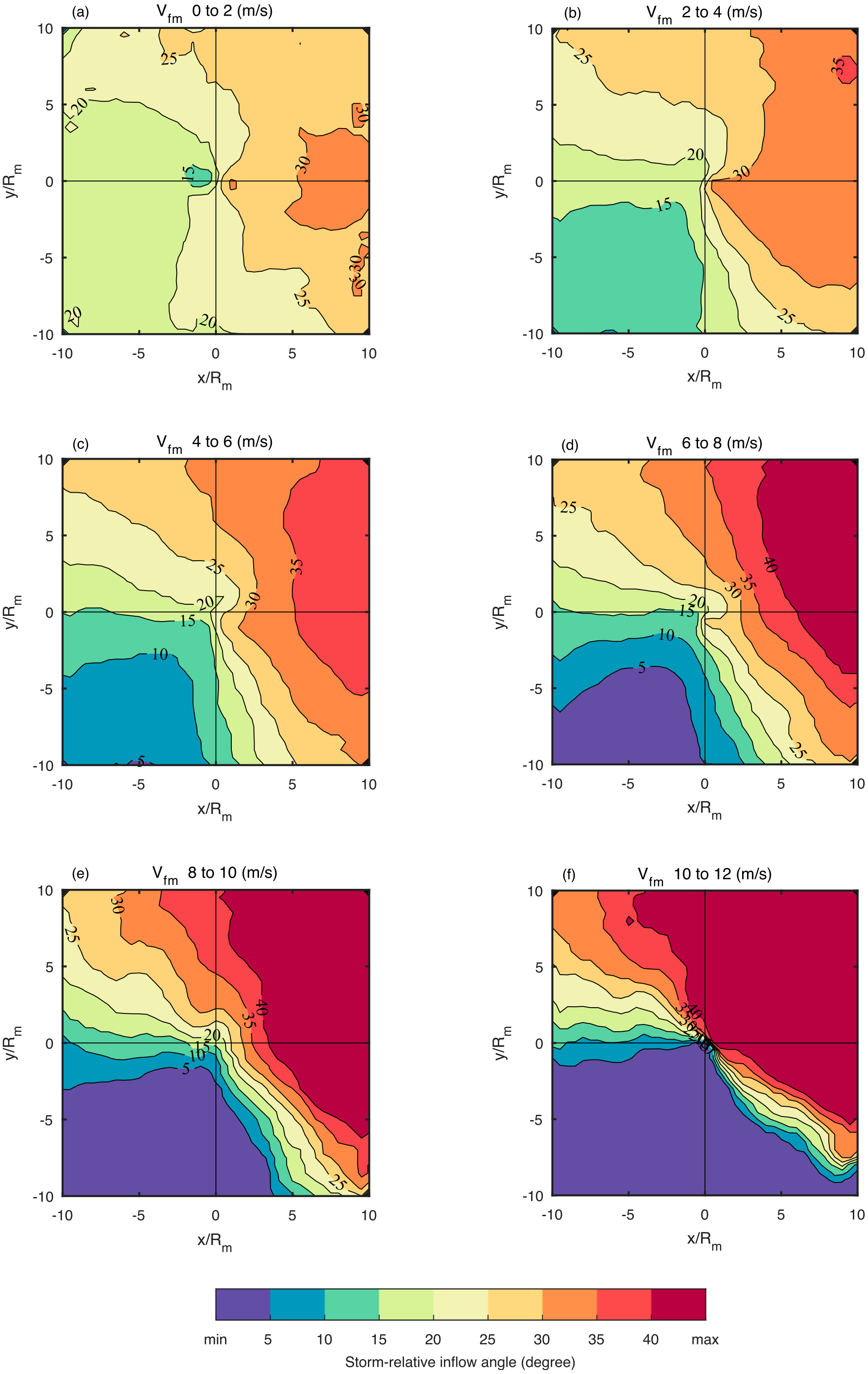

FIG. 16. Contours of tropical cyclone storm-relative wind inflow angle (°) from the full composite dataset of all tropical cyclones. Data are partitioned by velocity of forward movements V_{fm}: (a) 0–2, (b) 2–4, (c) 4–6, (d) 6–8, (e) 8–10, and (f) 10–12 m s^{-1}. Data are binned at $0.5R_m \times 0.5R_m$ resolution and tropical cyclone propagation north (toward the top of the page). Note the lowest and highest contours bands span from 5° to the lowest value recorded (−10°) and 40° to the highest value recorded (65°), respectively.

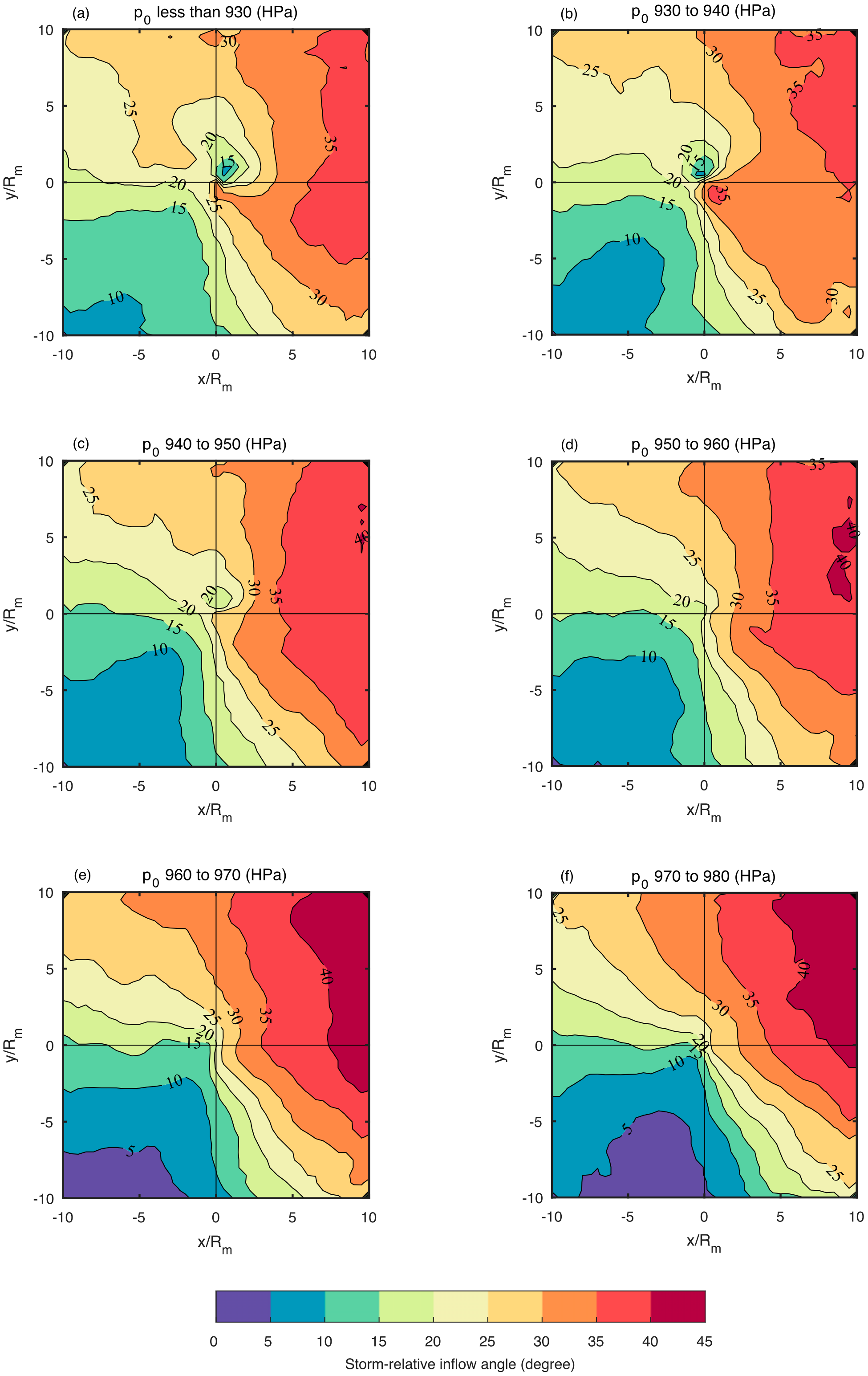

FIG. 17. Contours of tropical cyclone storm-relative wind inflow angle (°) from the full composite dataset of all tropical cyclones. Data are partitioned by central pressure p_0: (a) <930, (b) 930–940, (c) 940–950, (d) 950–960, (e) 960–970, and (f) 970–980 hPa. Data are binned at $0.5R_m \times 0.5R_m$ resolution and tropical cyclone propagation northward (up page).

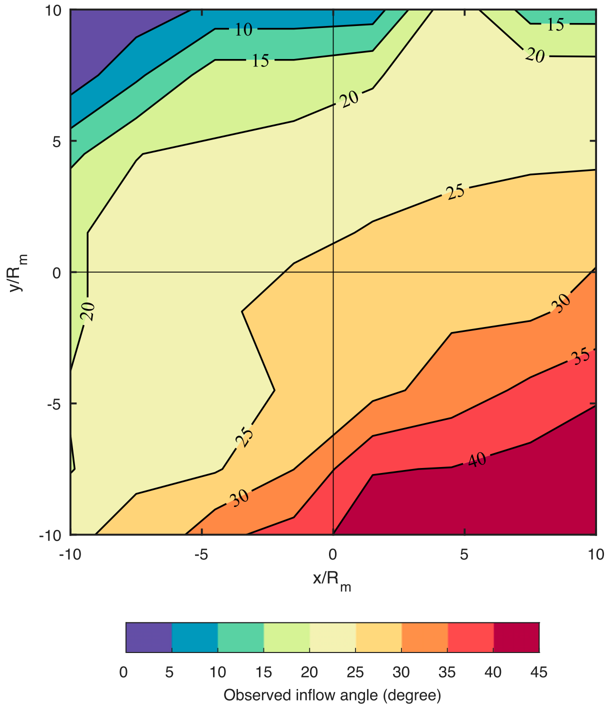

FIG. 18. Contours of tropical cyclone observed wind inflow angle (°) from the combined NDBC buoy dataset. Data are binned at $3R_m \times 3R_m$ resolution and tropical cyclone propagating northward (up page).

Similar to Fig. 14 (V_{fm} dependence), the observed inflow angle is approximately constant as a function of r for all octants with the exception of octants 7 and 8 (right-rear quadrant), where the observed inflow angle increases with increasing distance from the storm center, r.

Zhang and Uhlhorn (2012) found a weak dependence of the storm-relative inflow angle on storm intensity, with values of storm-relative inflow angle to the right of the storm center increasing slightly with storm intensity. This is very similar to the results in Fig. 17, where the maximum values of storm-relative inflow angle in the right-front quadrant increase from 35° for less intense storms (Fig. 17a) to 40° for more intense (smaller p_0) (Fig. 17f).

An independent potential validation dataset for the present scatterometer results is the National Data Buoy Center (NDBC) buoy data (Evans et al. 2003). Tamizi and Young (2020) compiled such a dataset consisting of all passes of North American hurricanes within $10R_m$ of such buoys since 1980. This dataset consists of a total of 353 hurricanes with 2902 passes. This results in a total of 19 057 observations of wind speed and direction. All data were corrected to a reference anemometer height of 10 m, assuming a neutral stability logarithmic boundary layer. Again, all data are referenced to the IBTrACS location of the storm center and rotated such that storms all propagate in the same direction. Although this is an extensive dataset, it is much smaller than the scatterometer dataset and hence the data needed to be binned at a coarser $3R_m \times 3R_m$ resolution. At such resolution, structure near the hurricane eye cannot be resolved but spatial distributions of wind speed and direction can be obtained farther from the eye (larger r/R_m). As for the scatterometer data, the median wind vector was determined for each $3R_m$ bin. Because of the more limited data, it was not possible to partition the data by p_0 or V_{fm}. The resulting values of the observed inflow angle from the full dataset (i.e., no partitioning) are shown in Fig. 18. The contour interval and color scale are the same as Figs. 14 and 15. The results are generally consistent with the scatterometer data, noting the reduced resolution. The buoy data again show the maximum observed inflow angle in the right-rear quadrant with maximum values of approximately 40° (cf. 35° for scatterometer). The minimum observed inflow angles occur in the left-front quadrant with values as small as 5° (as for scatterometer). Noting that the buoy data cannot resolve structure near the eye of the storm, the spatial variations are consistent with the scatterometer results.

Based on these comparisons we conclude that the buoy data supports the results from the extensive scatterometer dataset that the maximum observed inflow angles are in the right-rear quadrant.

6. Conclusions

The present analysis compiles a very large dataset of scatterometer passes over tropical cyclones. For tropical cyclones for which the central pressure, $p_0 < 980$ hPa and the velocity of forward movement, $V_{\mathrm{fm}} < 12\,\mathrm{m\,s^{-1}}$, there are a total of 9056 scatterometer overpasses of 592 tropical cyclones, producing a total of 9 904 738 wind speed and direction observations (Table 1). This large dataset enables the spatial distribution of the tropical cyclone wind speed and direction to be investigated and the dependence on central pressure and velocity of forward movement determined. The analysis calibrates the scatterometer wind speed data consistent with dropwindsonde data under tropical cyclone conditions (Chou et al. 2013) and bias corrects the resulting values. The bias correction is necessary as random errors in the tropical cyclone wind field parameters (particularly central position) impacts the winds of the composite wind fields. The corrected scatterometer data are validated against SFMR data from aircraft flights through North Atlantic hurricanes.

The spatial distributions of the wind fields show a clear left–right asymmetry with the maximum observed wind speed crescent directly right of the storm center. The asymmetry at $x/R_m \geq 2$ is approximately equal to the velocity of forward movement V_{fm}.

The observed wind inflow angles vary both radially and azimuthally and are a function of both V_{fm} and p_0. The largest observed inflow angles are found in the right-rear quadrant (~35°) and the smallest in the left-front quadrant (~10°). In all quadrants except the right-rear quadrant, the observed inflow angle is approximately constant as a function of the radial distance (r) from the storm center. In the right-rear quadrant, the observed inflow angle increases with r. With increasing V_{fm} the observed inflow angle ahead of the storm decreases and behind the storm increases. Similar changes occur as a function of p_0. As p_0 decreases, the observed inflow angle ahead of the storm decreases and that behind the storm increases.

The spatial distribution of the observed inflow angles is shown to be consistent with an independent NDBC buoy dataset. Storm-relative values of inflow angle are also shown to be consistent with previous, more limited, datasets.

Acknowledgments. The authors would like to acknowledge the support provide to AT by the University of Melbourne through a PhD scholarship. The development of the scatterometer database was supported by a grant from the Integrated Marine Observing System (IMOS). We would also like to thank the extremely helpful suggestions of Dr. Greg Holland, the reviewers and editor, which significantly enhanced the paper.

REFERENCES

Alves, J. H. G. M., and I. R. Young, 2003: On estimating extreme wave heights using combined Geosat, TOPEX/Poseidon and ERS-1 altimeter data. *Appl. Ocean Res.*, **25**, 167–186, https://doi.org/10.1016/j.apor.2004.01.002.

Bender, L. C., III, N. L. Guinasso Jr., J. N. Walpert, and S. D. Howden, 2010: A comparison of methods for determining significant wave heights—Applied to a 3-m discus buoy during Hurricane Katrina. *J. Atmos. Oceanic Technol.*, **27**, 1012–1028, https://doi.org/10.1175/2010JTECHO724.1.

Bessho, K., K. M. DeMaria, and J. A. Knaff, 2006: Tropical cyclone wind retrievals from the Advanced Microwave Sounding Unit: Application to surface wind analysis. *J. Appl. Meteor. Climatol.*, **45**, 399–415, https://doi.org/10.1175/JAM2352.1.

Biswas, M. K., and Coauthors, 2016: Hurricane Weather Research and Forecasting (HWRF) model: 2016 scientific documentation. Development Testbed Centre Rep., HWRF, 95 pp.

Brennan, M. J., C. C. Hennon, and R. D. Knabb, 2009: The operational use of QuikSCAT ocean surface vector winds at the National Hurricane Center. *Wea. Forecasting*, **24**, 621–645, https://doi.org/10.1175/2008WAF2222188.1.

Chou, K.-H., C.-C. Wu, and S.-Z. Lin, 2013: Assessment of the ASCAT wind error characteristics by global dropwindsonde observations. *J. Geophys. Res. Atmos.*, **118**, 9011–9021, https://doi.org/10.1002/jgrd.50724.

DiNapoli, S. M., M. A. Bouressa, and M. D. Powell, 2012: Uncertainty and intercalibration analysis of H*wind. *J. Atmos. Oceanic Technol.*, **29**, 822–833, https://doi.org/10.1175/JTECH-D-11-00165.1.

Evans, D., C. L. Conrad, and F. M. Paul, 2003: Handbook of automated data quality control checks and procedures of the National Data Buoy Center. NOAA/National Data Buoy Center Tech. Doc. 03-02, 44 pp.

Franklin, J. L., M. L. Black, and K. Valde, 2003: GPS dropwindsonde wind profiles in hurricanes and their operational implications. *Wea. Forecasting*, **18**, 32–44, https://doi.org/10.1175/1520-0434(2003)018<0032:GDWPIH>2.0.CO;2.

Hersbach, H., A. Stoffelen, and S. de Haan, 2007: An improved C-band scatterometer ocean geophysical modelfunction: CMOD5. *J. Geophys. Res.*, **112**, C03006, https://doi.org/10.1029/2006JC003743.

Holland, G., 1980: An analytic model of the wind and pressure profiles in hurricanes. *Mon. Wea. Rev.*, **108**, 1212–1218, https://doi.org/10.1175/1520-0493(1980)108<1212:AAMOTW>2.0.CO;2.

——, 2008: A revised hurricane pressure–wind model. *Mon. Wea. Rev.*, **136**, 3432–3445, https://doi.org/10.1175/2008MWR2395.1.

——, J. I. Belanger, and A. Fritz, 2010: A revised model for radial profiles of hurricane winds. *Mon. Wea. Rev.*, **138**, 4393–4401, https://doi.org/10.1175/2010MWR3317.1.

Houston, S. H., W. A. Shaffer, M. D. Powell, and J. Chen, 1999: Comparisons of HRD and SLOSH surface wind fields in hurricanes: Implications for storm surge modelling. *Wea. Forecasting*, **14**, 671–686, https://doi.org/10.1175/1520-0434(1999)014<0671:COHASS>2.0.CO;2.

Hu, K., Q. Chen, and S. K. Kimball, 2012: Consistency in hurricane surface wind forecasting: An improved parametric model. *Nat. Hazards*, **61**, 1029–1050, https://doi.org/10.1007/s11069-011-9960-z.

Irish, J. L., D. T. Resio, and J. J. Ratcliff, 2008: The influence of storm size on hurricane surge. *J. Phys. Oceanogr.*, **38**, 2003–2013, https://doi.org/10.1175/2008JPO3727.1.

Jensen, R., V. Swail, R. Bouchard, R. Riley, T. Hesser, M. Blaseckie, and C. MacIsaac, 2015: Field laboratory for Ocean Sea State Investigation and Experimentation: FLOSSIE: Intra-measurement evaluation of 6N wave buoy systems. *14th Int. Workshop on Wave Hindcasting and Forecasting/Fifth Coastal Hazard Symp.,* Key West, FL, WMO/IOC JCOMM, A1, 19 pp., http://www.waveworkshop.org/14thWaves/Papers/WW14%20FLOSSIE%20Jensen%20et%20al.pdf.

Kepert, J., 2006a: Observed boundary layer wind structure and balance in the hurricane core. Part I: Hurricane Georges. *J. Atmos. Sci.*, **63**, 2169–2193, https://doi.org/10.1175/JAS3745.1.

——, 2006b: Observed boundary layer wind structure and balance in the hurricane core. Part II: Hurricane Mitch. *J. Atmos. Sci.*, **63**, 2194–2211, https://doi.org/10.1175/JAS3746.1.

——, and Y. Wang, 2001: The dynamics of boundary layer jets within the tropical cyclone core. Part II: Nonlinear enhancement. *J. Atmos. Sci.*, **58**, 2485–2501, https://doi.org/10.1175/1520-0469(2001)058<2485:TDOBLJ>2.0.CO;2.

Kimball, S. K., and M. S. Mulekar, 2004: A 15-year climatology of North Atlantic tropical cyclones. Part I: Size parameters. *J. Climate*, **17**, 3555–3575, https://doi.org/10.1175/1520-0442(2004)017<3555:AYCONA>2.0.CO;2.

Klotz, B. W., and H. Jiang, 2016: Global composites of surface wind speeds in tropical cyclones based on a 12-year scatterometer database. *Geophys. Res. Lett.*, **43**, 10 480–10 488, https://doi.org/10.1002/2016GL071066.

——, and ——, 2017: Examination of surface wind asymmetries in tropical cyclones. Part I: General structure and wind shear impacts. *Mon. Wea. Rev.*, **145**, 3989–4009, https://doi.org/10.1175/MWR-D-17-0019.1.

Knapp, K. R., H. J. Diamond, J. P. Kossin, M. C. Kruk, and C. J. Schreck, 2018:International Best Track Archive for Climate Stewardship (IBTrACS) Project, Version 4. NOAA/National Centers for Environmental Information, accessed 10 October 2019, https://doi.org/10.25921/82ty-9e16.

Mehra, A., V. Tallapragada, Z. Zhang, B. Liu, L. Zhu, W. Wang, and H.-S. Kim, 2018: Advancing the state of the art in operational tropical cyclone forecasting at NCEP. *Trop. Cyclone Res. Rev.*, **7**, 51–56.

Olfateh, M., D. P. Callaghan, P. Nielsen, and T. E. Baldock, 2017: Tropical cyclone wind field asymmetry—Development and evaluation of a new parametric model. *J. Geophys. Res. Oceans.*, **122**, 458–469, https://doi.org/10.1002/2016JC012237.

Powell, M. D., 1982: The transition of the Hurricane Frederic boundary-layer wind field from the open Gulf of Mexico to landfall. *Mon. Wea. Rev.*, **110**, 1912–1932, https://doi.org/10.1175/1520-0493(1982)110<1912:TTOTHF>2.0.CO;2.

——, and S. H. Houston, 1996: Hurricane Andrew's landfall in South Florida. Part II: Surface wind fields and potential real-time applications. *Wea. Forecasting*, **11**, 329–349, https://doi.org/10.1175/1520-0434(1996)011<0329:HALISF>2.0.CO;2.

——, ——, L. R. Amat and N. Morisseau-Leroy, 1998: The HRD real-time hurricane wind analysis system. *J. Wind Eng. Ind.*

Aerodyn., **77–78**, 53–64, https://doi.org/10.1016/S0167-6105%2898%2900131-7.

——, P. J. Vickery, and T. A. Reinhold, 2003: Reduced drag coefficient for high wind speeds in tropical cyclones. *Nature*, **422**, 279–283, https://doi.org/10.1038/nature01481.

——, and Coauthors, 2010: Reconstruction of Hurricane Katrina's wind fields for storm surge and wave hindcasting. *Ocean Eng.*, **37**, 26–36, https://doi.org/10.1016/j.oceaneng.2009.08.014.

Ribal, A., and I. R. Young, 2020: Calibration and cross-validation of global ocean wind speed based on scatterometer observations. *J. Atmos. Oceanic Technol.*, **37**, 279–297, https://doi.org/10.1175/JTECH-D-19-0119.1.

Ruf, C. S., and Coauthors, 2016: New ocean winds satellite mission to probe hurricanes and tropical convection. *Bull. Amer. Meteor. Soc.*, **97**, 385–395, https://doi.org/10.1175/BAMS-D-14-00218.1.

Schwendike, J., and J. D. Kepert, 2008: The boundary layer winds in Hurricanes Danielle (1998) and Isabel (2003). *Mon. Wea. Rev.*, **136**, 3168–3192, https://doi.org/10.1175/2007MWR2296.1.

Shapiro, J. J., 1983: The asymmetric boundary layer under a translating hurricane. *J. Atmos. Sci.*, **40**, 1984–1998, https://doi.org/10.1175/1520-0469(1983)040<1984:TABLFU>2.0.CO;2.

Shea, D. J., and W. M. Gray, 1973: The hurricane's inner core region. I: Symmetric and asymmetric structure. *J. Atmos. Sci.*, **30**, 1544–1564, https://doi.org/10.1175/1520-0469(1973)030<1544:THICRI>2.0.CO;2.

Sun, Z., B. Zhang, J. A. Zhang, and W. Perrie, 2019: Examination of surface wind asymmetry in tropical cyclones over the Northwest Pacific Ocean using SMAP observations. *Remote Sens.*, **11**, 2604, https://doi.org/10.3390/rs11222604.

Tamizi, A., and I. R. Young, 2020: The spatial distribution of ocean waves in tropical cyclones. *J. Phys. Oceanogr.*, **50**, 2123–2139, https://doi.org/10.1175/JPO-D-20-0020.1.

Ueno, M., and K. Bessho, 2011: A statistical analysis of near-core surface wind asymmetries in typhoons obtained from QuikSCAT data. *J. Meteor. Soc. Japan*, **89**, 225–241, https://doi.org/10.2151/jmsj.2011-304.

Uhlhorn, E. W., P. G. Black, J. L. Franklin, M. Goodberlet, J. Carswell, and A. S. Goldstein, 2007: Hurricane surface wind measurements from an operational stepped frequency microwave radiometer. *Mon. Wea. Rev.*, **135**, 3070–3085, https://doi.org/10.1175/MWR3454.1.

——, B. W. Klotz, T. Vukicevic, P. D. R. Easor, and R. F. Rogers, 2014: Observed hurricane wind speed asymmetries and relationships to motion and environmental shear. *Mon. Wea. Rev.*, **142**, 1290–1311, https://doi.org/10.1175/MWR-D-13-00249.1.

Verhoef, A., M. Portabella, and A. Stoffelen, 2012: High-resolution ASCAT scatterometer winds near the coast. *IEEE Trans. Geosci. Remote Sens.*, **50**, 2481–2487, https://doi.org/10.1109/TGRS.2011.2175001.

Willoughby, H. E., R. W. R. Darling, and M. E. Rahn, 2006: Parametric representation of the primary hurricane vortex. Part II: A new family of sectionally continuous profiles. *Mon. Wea. Rev.*, **134**, 1102–1120, https://doi.org/10.1175/MWR3o106.1.

Xie, L., S. Bao, L. J. Pietrafesa, K. Foley, and M. Fuentes, 2006: A real-time hurricane surface wind forecasting model: Formulation and verification. *Mon. Wea. Rev.*, **134**, 1355–1370, https://doi.org/10.1175/MWR3126.1.

Young, I. R., 1998: Observations of the spectra of hurricane generated waves. *Ocean Eng.*, **25**, 261–276, https://doi.org/10.1016/S0029-8018(97)00011-5.

——, 2006: Directional spectra of hurricane wind-waves. *J. Geophys. Res.*, **111**, C08020, https://doi.org/10.1029/2006JC003540.

——, 2017: A review of parametric descriptions of tropical cyclone wind-wave generation. *Atmosphere*, **8**, 194, https://doi.org/10.3390/atmos8100194.

——, and J. Vinoth, 2013: An 'extended fetch' model for the spatial distribution of tropical cyclone wind-waves as observed by altimeter. *Ocean Eng.*, **70**, 14–24, https://doi.org/10.1016/j.oceaneng.2013.05.015.

Zhang, J., and E. W. Uhlhorn, 2012: Hurricane sea surface inflow angle and an observation-based parametric model. *Mon. Wea. Rev.*, **140**, 3587–3605, https://doi.org/10.1175/MWR-D-11-00339.1.